The Electronic Structure of MAPI-Based Perovskite Solar Cells: Detailed Band Diagram Determination by Photoemission Spectroscopy Comparing Classical and Inverted Device Stacks

Tim Hellmann, Chittaranjan Das, Tobias Abzieher, Jonas A. Schwenzer, Michael Wussler, Ralph Dachauer, Ulrich W. Paetzold, Wolfram Jaegermann, and Thomas Mayer*

High power conversion efficiency (PCE) perovskite solar cells (PSCs) rely on optimal alignment of the energy bands between the perovskite absorber and the adjacent charge extraction layers. However, since most of the materials and devices of high performance are prepared by solution-based techniques, a deposition of films with thicknesses of a few nanometers and therefore a detailed analysis of surface and interface properties remains difficult. To identify the respective photoactive interfaces, photoelectron spectroscopy measurements are performed on device stacks of methylammonium-lead-iodide (MAPI)-based PSCs in classical and inverted architectures in the dark and under illumination at open-circuit conditions. The analysis shows that vacuum-deposited MAPI perovskite absorber layers are n-type, independent of the architecture and of the charge transport layer that it is deposited on (n-type SnO_2 or p-type NiO_x). It is found that the majority of the photovoltage is formed at the n-MAPI/p-HEL (hole extraction layer) junction for both architectures, highlighting the importance of this interface for further improvement of the photovoltage and therefore also the PCE. Finally, an experimentally derived band diagram of the completed devices for the dark and the illuminated case is presented.

T. Hellmann, Dr. C. Das, M. Wussler, Dr. R. Dachauer,
Prof. W. Jaegermann, Dr. T. Mayer
Surface Science Group
Materials Science Department
Technical University of Darmstadt
Alarich-Weiss-Straße 2, 64287 Darmstadt, Germany
E-mail: mayerth@surface.tu-darmstadt.de
Dr. T. Abzieher, Dr. J. A. Schwenzer, Dr. U. W. Paetzold
Light Technology Institute
Karlsruhe Technology Institute
Engesserstraße 13, 76131 Karlsruhe, Germany
Dr. U. W. Paetzold
Institute of Microstructure Technology
Karlsruhe Institute of Technology
Hermann-von-Helmholtz-Platz 1
76344 Eggenstein-Leopoldshafen, Germany

1. Introduction

Organic–inorganic lead halide perovskite solar cells (PSCs) have been intensively studied over the past decade, reaching record power conversion efficiencies (PCEs) of more than 25%.[1] In addition, encouraging progress has also been demonstrated in terms of low-cost upscaling deposition and improved stability that may allow commercialization of this ambitious technology in the near future.[2] To further advance the PCE, it is of fundamental interest to investigate the given band energy diagram, by identifying the interface at which the photovoltage inside the PSC develops. The working principle of this kind of solar cell is still a topic of extensive scientific debate requiring more experimental evidence to arrive at more definitive conclusions.

PSCs are commonly distinguished into two different architectures: i) the classical architecture (also called n-i-p structure), where the front contact is an n-type electron extraction layer (EEL) and the back contact is a p-type hole extraction layer (HEL) and ii) the inverted architecture (also referred to as p-i-n structure), where the n-EEL and the p-HEL are exchanged. For a PSC with an intrinsic perovskite absorber, the built-in potential in the dark and the photovoltage under illumination will be formed at both the n-EEL/i-perovskite interface and at the i-perovskite/p-HEL interface. Understanding the device physics and especially the band alignment across the interfaces will help to identify strategies to improve PSCs. This knowledge can trigger the development of new charge extraction layers that can form suitable interfaces to the perovskite absorber to maximize the open-circuit voltage (V_{OC}) and thus the PCE.[3–8] Up to date, large efforts have been made to further boost the PCE by using various EELs[9] and HELs[6,10–13] or by exchanging the metal contacts,[14] however, due to a lack of knowledge about the energy band diagram, often on an empirical basis without generalized guidelines.

Kelvin probe force microscopy (KFPM) and electron-beam-induced current (EBIC) measurements have been performed

ADVANCED
SCIENCE NEWS
www.advancedsciencenews.com

ADVANCED
ENERGY
MATERIALS
www.advenergymat.de

to help identifying at which interfaces a built-in potential exists in the dark and a photovoltage is generated under illumination.[15–19] However, in KFPM measurements the position of the Fermi level in the energy gap of the different layers and the electronic structure including the band line up and band bending at the interfaces can only be concluded from the variation of the work function throughout the device.

In 2014, Edri et al.[15] performed EBIC measurements on cross-sections of classical architecture devices using TiO$_2$ as EEL and spiro-MeOTAD as HEL. The authors there found two humps of EBIC in the methylammonium-lead-iodide (MAPI) near the contacts and stated that this is typically found for a p-i-n structure, with MAPI being the intrinsic absorber. While we agree that a p-i-n structure leads to two humps in EBIC, we believe that other structures can do so as well. For example, an n-doped instead of an intrinsic perovskite, will results in a similar EBIC shape, if the contact layers act as efficient electron bocking HEL and hole blocking EEL. Similarly, Bergmann et al. performed KFPM measurements on cross-sections of completed devices and interpreted the contact potential distribution corresponding to a p-i-n-structure.[16] Cai et al. could move the potential drop from the TiO$_2$/MAPI interface to the MAPI/spiro-MeOTAD interface by changing the PbI$_2$ to MAI ratio of the MAPI precursor solution and thereby the thereby the n- or p-doping level of the MAPI film.[20] This is to be expected, since it has been reported that the doping of the perovskite can be influenced by controlling its PbI$_2$ to MAI ratio either pre-depositional in the precursor solution or post-depositonal by annealing.[21–24]

In contrast to KFPM, photoelectron spectroscopy (PES) allows to directly measure the electronic structure as well as the chemical state of the material. Under illumination, the surface photovoltage (SPV) can be measured as well, if the sample is grounded adequately. The SPV is a potential difference between the surface Fermi level of the sample stack and its back contact connected to the ground of the X-ray photoelectron spectroscopy (XPS) system. It usually results from the separation of photogenerated charge carriers via a built-in field at one of the interfaces inside the sample.[25,26] Since the SPV corresponds to the V_{OC} of the device, identifying the interfaces at which the SPV and therefore the V_{OC} develope will help to further improve the device performance. The SPV is visible in PES by the shift of all emission lines from their electronic equilibrium conditions in the dark to higher or lower binding energies, depending if it is a positive or negative SPV, respectively. PES studies of MAPI do often report a substrate-dependent Fermi level position of MAPI. For n-type substrates, the Fermi level of MAPI is often reported close to the conduction band minimum (CBM), while it is observed in the middle of the band gap for p-type substrates.[27–30] Zu et al. observed that the perovskite is n-type on p-type poly(triaryl) amine (PTAA) substrates in the dark and the perovskite appears intrinsic under illumination, due to the formation of an SPV. They argued that the perovskite is p-type in the bulk with a downward band bending at the MAPI/vacuum surface that makes the surface to appear n-type.[31] However, with their experiments they could not verify if the involved SPV appears at the MAPI/vacuum surface or at a different interface below.

To contribute toward clarifying these controversially discussed results, specifically designed experiments are presented in this work. XPS and ultraviolet photoelectron spectroscopy (UPS) measurements in the dark and under illumination are used on different device stacks in classical architecture (front contact: n-SnO$_2$) and inverted device architecture (front contact: p-NiO$_x$), keeping the device at open-circuit condition, and making a direct comparison for the distribution of the photovoltage of both architectures. In addition, full devices are prepared with the vacuum-deposited MAPI films with stabilized efficiencies of 13.7% and 11.6% for the inverted and classical solar cells (see Figure S1, Supporting Information). The interfaces where the photovoltages appear, are analyzed in more detail, either by classical step-by-step interface experiments[32] or by preparing and measuring a tapered cross-section.[33] For both architectures, it is proven that at the interfaces where the SPV forms under illumination, a built-in potential exists in the dark. As a result, for both architectures the used MAPI films are observed to be n-type in the dark, independent of the substrate (EEL or HEL) that they are deposited on. Under illumination, an SPV for MAPI on the p-type substrate (p-NiO$_x$) is observed, which shifts the Fermi level to appear in the middle of the band gap. For MAPI on the n-type substrate (n-SnO$_2$) no light-induced SPV is observed and only after depositing the p-type layer on top of MAPI the SPV appears. For both architectures, the photovoltage is therefore identified at the p-HEL/n-MAPI heterojunction. It is further concluded that the investigated devices are working as n$^+$-n-p-devices for the classical and as p-n-n-devices for the inverted architecture as compared to the n-i-p-structure or p-i-n-structure, that is often assumed in literature. To further improve the V_{OC} and therefore the PCE of PSCs, it is therefore recommended to focus on optimizing the interface properties of the n-MAPI/p-HEL interface. The importance of the n-MAPI/p-HEL interface might also explain, why many of the recently reported passivation layers that are used to improve the PCE are employed in between the perovskite absorber and the HEL.[34–38]

2. Results

2.1. Laying Out the Strategy: How to Determine the Band Structure using PES

In this work, the energy band diagram of devices in classical and inverted architecture is determined and directly compared. The layer stack sequences that are used for both architectures are displayed in **Figure 1**a. For the classical architecture, the layer stack sequence indium tin oxide (ITO)/n$^+$-SnO$_2$/MAPI/p-spiro-MeOTAD/Au is employed, whereas for the inverted architecture the sequence ITO/p-NiO$_x$/MAPI/C$_{60}$/bathocuproine (BCP)/Au is used. The letters "n-" and "p-" are used in this work to describe whether the respective material is an EEL (e.g., n-SnO$_2$) or an HEL (e.g., p-NiO$_x$). An illuminated sample during the PES measurement is illustrated in Figure 1b. The ITO layer is connected to the electrical ground of the XPS machine, which means that the potentials of all other layers on top are electrically floating and an SPV between the ITO front contact and the top layer can build up. The effect of an SPV under illumination
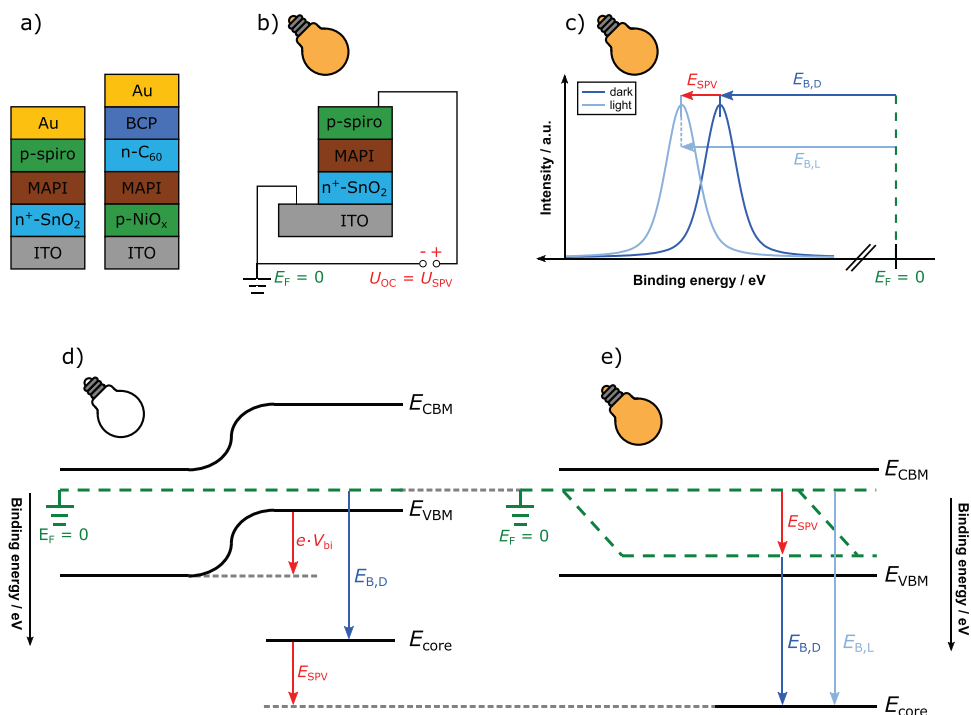
Figure 1. a) Classical (left) and inverted (right) layer stack sequences employed in this work, b) an illuminated layer stack during the PES measurement with an SPV formed in the classical layer stack, and c) the resulting shift (E_{SPV}) of a core level emission line due to the light-induced SPV. $E_{B,D}$ and $E_{B,L}$ represent the binding energies in the dark and under illumination, respectively. A theoretical p-n-junction in the dark with d) the built-in potential V_{bi} and e) under illumination with the formed photovoltage E_{SPV}.

on the PES spectra is presented in Figure 1c, where the positive SPV shifts the core level emission line of the measured top layer to higher binding energies.[25,26] Respectively, a negative SPV would result in a shift of the emission lines to lower binding energies. Similar dark and light measurements for MAPI films on n^+-SnO$_2$ and p-NiO$_x$ substrates are presented in the first section of this work together with a discussion of the influence of both substrates on the electronic structure of the MAPI films and a potential SPV. Then, similar measurements on the respective back contact layer (spiro-MeOTAD and BCP) and on finished device stacks with a gold electrode on top are discussed. The experimental sample sequence is chosen in a way that by comparing the dark and light measurements, the interface at which the photovoltage is formed can be identified unambiguously and compared for both architectures. Schematic band diagrams in the dark and under illumination are shown in Figure 1d,e, for a simple n-p-junction. In the dark case, a built-in potential (V_{bi}, band bending) that limits the magnitude of the SPV must be present. During the light measurements, the excited charge carriers result in a splitting of the electron and hole quasi-Fermi levels and the formed SPV will reduce the built-in potentials, approaching a flat-band situation. Since in PES the reference Fermi level is fixed by grounding the substrate, the quasi-Fermi level shift appears as a shift of all core level emission lines and the valence band region to higher binding energies. It should be noted that an unnoticed SPV due to unintentional illumination can result in misinterpretation of the data in PES, since in the nonequilibrium situation spectra will be shifted.[26,39,40] Therefore, extreme care has been taken to avoid unintentional illumination during the dark

measurements. The induced change in the valence band position with respect to the Fermi level reference would result in a wrong doping level assignment. In the third part, the results from the PES measurements are used to construct full energy band diagrams in the dark and under illumination for the classical and inverted architecture.

2.2. Electronic Structure of MAPI Thin Films on Different Substrates

First, the influence of the substrate on the Fermi level position of the perovskite absorber is investigated and potential SPVs at the interface between the front contact and the perovskite absorber are identified. The following XPS measurements will provide evidence that the Fermi level position of the deposited perovskite absorber is n-type, independent of the substrate when measured in the dark. Additional X-ray diffraction (XRD) and UV/vis measurements of the perovskite films on SnO$_2$ and NiO$_x$ are supplied in Figure S2 in the Supporting Information. The XRD shows in addition to the MAPI diffraction peaks only small PbI$_2$ peaks on SnO$_2$, which are even smaller on NiO$_x$.

PES measurements on n^+-SnO$_2$/MAPI and p-NiO$_x$/MAPI stacks are performed in the dark and under illumination. **Figure 2** shows the XPS data of vacuum-deposited MAPI films for the classical architecture (grown on SnO$_2$ substrates) (a to c) and for the inverted architecture grown on NiO$_x$ substrates (d to f). The valence band regions are displayed with a logarithmic intensity scale. Often, the valence band maximum (VBM) of a semiconductor is determined from a plot with a
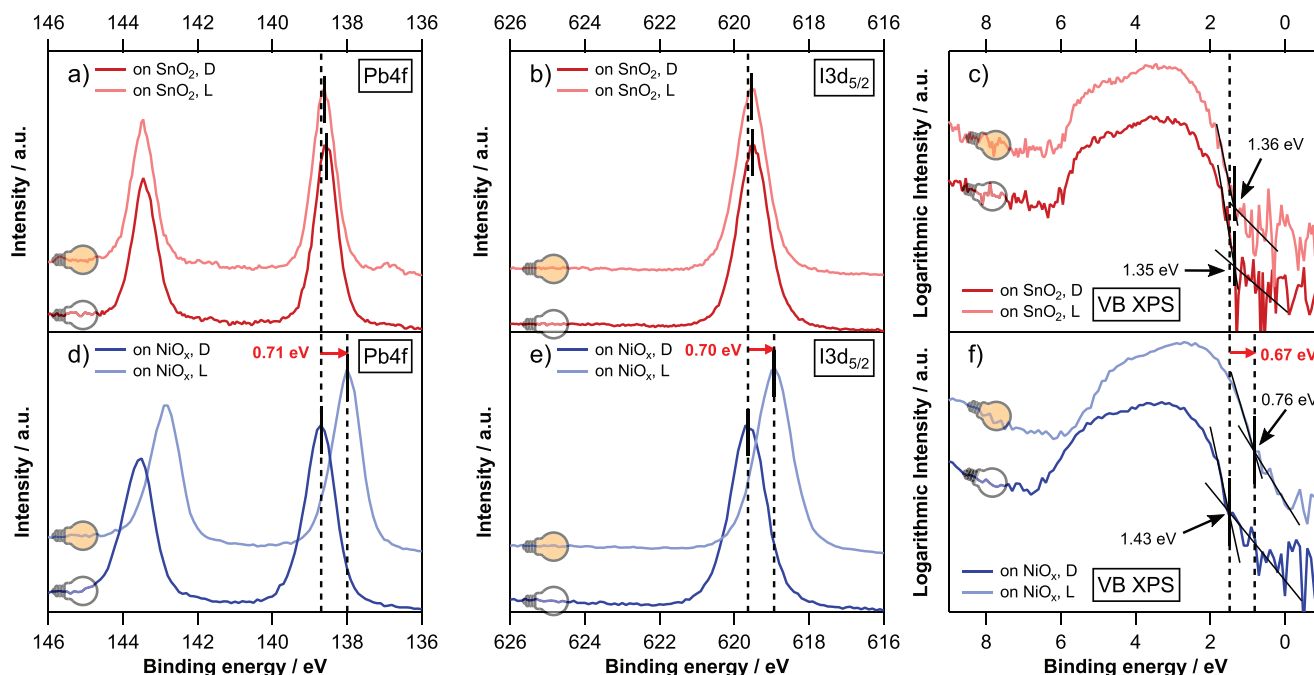
Figure 2. a–c) (red curves) Detailed Pb4f scans, I3d$_{5/2}$ scans, and valence band scans of MAPI films grown on SnO$_2$ in the classical architecture and d–f) (blue curves) on NiO$_x$ in the inverted architecture. The indices "D" and "L" and the light bulbs indicate whether the measurement was performed in the dark or under illumination. The scale of the binding energy axis of all three figures is set to 10 eV to allow a better comparison of the light-induced shifts.

linear intensity scale, by applying a linear fit to the leading edge of the valence band spectrum and determining the intersection with zero counts. However, for organic–inorganic lead halide perovskite like MAPI, Endres et al. reported an unusually low density of states (DOS) at the valence band edge,[41] which can result in an erroneous estimation of the VBM binding energy, when it is determined from a plot with linear intensity scale. This error may be avoided by using a logarithmic intensity scale, which enhances the low DOS at the valence band edge. Reported values for the VBM of MAPI vary from 1.15 to 1.40 eV[41–43] when the value is determined from a logarithmic intensity plot and are as high as 1.55 eV[29] or even 1.78 eV[28] when a linear intensity plot is used. In this work, the VBM values of the perovskite absorbers were determined from a logarithmic intensity plot since this method seems to give the more reliable values. To exclude that the VBM is misinterpreted by surface contaminations due to the samples being handled in ambient atmosphere, a reference perovskite sample was prepared inside the vacuum and measured without exposing it to the ambient atmosphere. The distances between the core levels and the VBM ($\Delta E_{B,I3d5/2} = 618.10$ eV and $\Delta E_{B,Pb4f7/2} = 137.19$ eV) are then compared to the other perovskite samples, since these values are material constants. A more detailed discussion on the determination of the VBM of the perovskite absorber is given in the Supporting Information (see Figure S3). For the classical architecture in the dark, the VBM of MAPI is located 1.35 eV below the Fermi level (see Figure 2c) indicating an n-type character as the band gap is 1.58 eV. The Pb4f$_{7/2}$ emission line (see Figure 2a) appears at 138.56 eV and the I3d$_{5/2}$ emission at 619.50 eV (see Figure 2b), which is in accordance with literature values for MAPI grown on n-type substrates.[44–46] The

core level to valence band distances of the I3d$_{5/2}$ emission line (618.22 eV) and the Pb4f$_{7/2}$ emission line (137.28 eV) are close to the values that were determined for the in-vacuo prepared reference sample ($\Delta E_{B,I3d5/2} = 618.10$ eV and $\Delta E_{B,Pb4f7/2} = 137.19$ eV, see Table S1, Supporting Information). Under illumination, the Pb4f$_{7/2}$ emission line appears at a binding energy of 138.61 eV (see Figure 2a), the I3d$_{5/2}$ emission at 619.54 eV (see Figure 2b), and the VBM at 1.36 eV (see Figure 2c). The shift of around 0.03 eV to higher binding energies is negligible and it is assumed that the light has almost no effect on the binding energy positions. Since there is no light-induced shift, it can directly be concluded that no SPV is forming at the n$^+$-SnO$_2$/n-MAPI interface. This is expected, given that the work functions of SnO$_2$ (4.15 eV) and MAPI (4.02 eV) are close to each other (see Figure S4, Supporting Information), meaning that no built-in potential should form at this contact.

For the inverted architecture in Figure 2d–f in the dark, the Pb4f$_{7/2}$ and I3d$_{5/2}$ emission lines and the VBM appear at about 0.1 eV higher binding energies as compared to the classical architecture, indicating an n-type MAPI as well. MAPI is therefore observed to be n-type, independent of the substrate material (n$^+$-SnO$_2$ or p-NiO$_x$) it is deposited on. After turning on the light, the Pb4f$_{7/2}$ and I3d$_{5/2}$ emission line and the VBM are shifting by 0.70 eV toward lower binding energies. A similar shift to lower binding energies appears for four other perovskites (FAPI, CsFAPI, MAFAPI, and CsMAFAPI) when spin-coated on NiO$_x$ as well (see Figure S5b, Supporting Information). With these perovskite absorbers used in solar cells, efficiencies of 16.4%, 17.0%, 19.2%, and 17.4% were obtained. When the four perovskites are spin-coated on SnO$_2$ instead, no light-induced shift is observed (see Figure S5a, Supporting Information) indicating
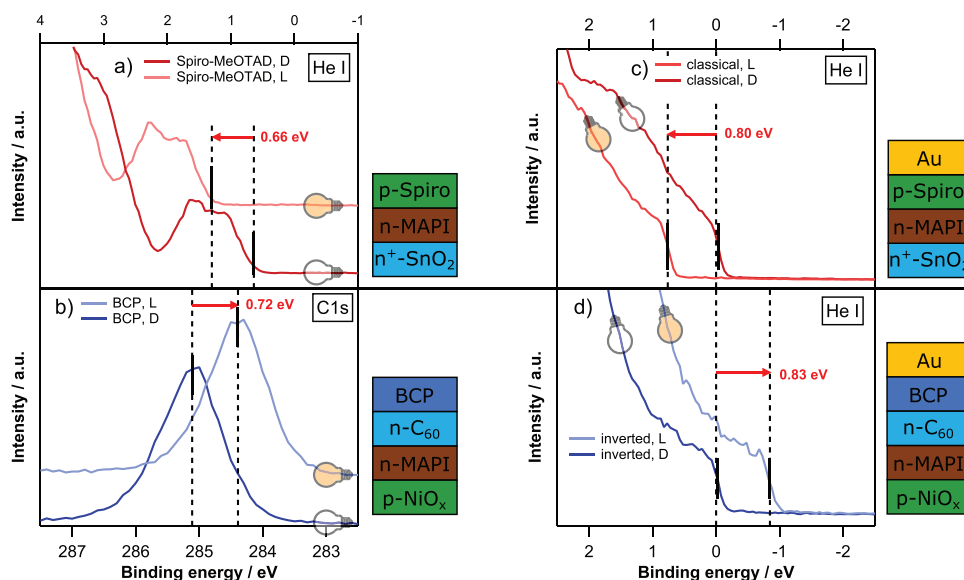
Figure 3. a) He I scans of a spiro-MeOTAD film deposited on top of the SnO_2/MAPI stack, b) C1s scans of a BCP film that was evaporated on top of a NiO_x/MAPI/C_{60} stack, and He I scans of completed devices in the c) classical and d) inverted structure. The letters "D" and "L" indicate whether the measurement was performed in the dark or under illumination. The scale of the binding energy axis of all figures is set to 10 eV to allow a better comparison of the light-induced shifts.

that the observed shift is not a measurement artifact of this specific sample but rather a general behavior of organic–inorganic lead halide perovskites. Since this shift on p-NiO_x substrates appears for both the vacuum-deposited and spin-coated perovskite films, it can be excluded that the deposition process has an influence on the interface at which the photovoltage appears. This is important to note, since it is known, that the direct co-evaporation of MAPI on metal oxides can result in nonstoichiometric growth in the initial nanometers. For example, PbI_2 or PbO may form initially.[28] The light-induced shift of the different perovskites on p-NiO_x is attributed to the formation of a SPV at the p-NiO_x/n-MAPI interface. Under illumination, the binding energy positions of the perovskite absorber appear at positions that indicate an intrinsic MAPI, but this is only caused by the SPV-induced shift and therefore a non-equilibrium situation of the perovskite film as it was schematically described in Figure 1e. Considering the high work function difference between MAPI (4.16 eV) and NiO_x (5.41 eV) (see Figure S4, Supporting Information), the formation of a built-in potential in the dark at this interface is expected. In a detailed analysis performed on the NiO_x/MAPI interface using a tapered cross-section approach,[33] the presence of a band bending inside the MAPI and thus a built-in potential at this interface is demonstrated (see Figure S6, Supporting Information). Under illumination, this built-in potential acts as driving force for the extraction of the excited holes out of the perovskite absorber into the underlying NiO_x layer which results in a negative SPV and therefore a shift of the core levels and the valence band to lower binding energies. It should be noted that Zu et al. also observed a light-induced shift to lower binding energies, when performing PES measurements on different perovskite absorbers deposited on p-PTAA substrates but explained it with a p-type bulk of the perovskite and a downward band bending at the MAPI/vacuum surface that makes the surface appear n-type.[31] Based on the more detailed

analysis provided in this work, the band bending appears at the p-HEL/n-MAPI interface instead. Having the photovoltage at the interface between the perovskite absorborber and the HEL will be proven using the classical architecture, where the SPV is shown to appear at the n-MAPI/p-spiro-MeOTAD interface (see **Figure 3**a), and therefore the n-MAPI/p-HEL interface as well. It is emphasized at this point that with the PES setup used in this work, even exceedingly small amounts of background light resulted in an SPV and consequently a shift of all PES spectra toward lower binding energies. For this reason, it was necessary to turn off the pressure gauge inside the measurement chamber and to use an Al window in between the X-ray source and the sample to avoid that scattered light can reach the sample and thereby distort the results. In literature, even X-ray-source-induced photovoltages have been observed.[26,39,40] Experimental PES data of perovskite absorbers can therefore be very easily misinterpreted if the background-light-induced SPV is not considered, which might be the case for other studies reported in literature. However, it can be excluded that the X-ray source or UPS lamp gives rise to an SPV, since the Fermi level of the Au back contact of the full device appears at the expected value of 0 eV (see Figure 3c,d) and only shifts when the external light source is turned on. There are XPS studies on MAPI films on top of p-HEL substrates in literature that report a Fermi level of the perovskite positioned in the middle of the band gap and therefore a more intrinsic MAPI layer. This intrinsic appearance of MAPI is usually explained by a substrate effect. A group performed PES measurements to investigate the electronic properties of MAPI depending on the substrate and found a VBM of 1.55 eV for n-TiO_2, 1.58 eV for n-ZnO, 0.84 eV for p-MoO_3, and 0.95 eV for p-PEDOT:PSS (poly(3,4-ethylenedioxythiophene):polystyrene sulfonate).[29] Similarly, a VBM of 1.4 eV for MAPI on n-TiO_2 and a slightly p-type MAPI with a VBM of 0.7 eV on p-NiO_x were reported using UPS.[47] Other publications reported VBM values
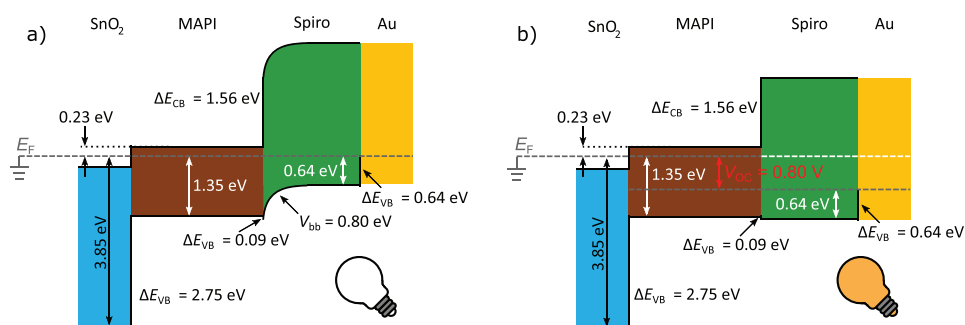
Figure 4. Schematic band diagrams derived from the PES measurements for devices in classical architecture. a) In the dark with band bending at the MAPI/spiro-MeOTAD interface and b) under illumination with the band bending changing to a flat-band situation, giving rise to the V_{OC}. The white horizontal extension of the Fermi level in b) shows the Fermi level of the ground and therefore the reference energy for the PES measurements.

between 0.9 and 1.38 eV for p-type substrates and 1.69–1.77 eV for n-type substrates[27] or a VBM of 1.78 eV for MAPI grown on n-PEIE (polyethyleneimine) and 1.24 or 1.14 eV for p-MoO$_3$ and p-PEDOT:PSS when using UPS, respectively.[28] According to the findings presented in this work, it should be considered that literature reports of intrinsic MAPI films on p-HEL substrates are n-type MAPI films as well, but with an unnoticed SPV, which results in a misinterpretation of the PES spectra.

Based on the presented experiments, it was clearly shown that the doping of the substrate has no or only negligible influence on the Fermi level position of MAPI and that MAPI thin films are n-type on n$^+$-SnO$_2$ as well as on p-NiO$_x$ substrates. On p-NiO$_x$ substrates, measurements under illumination result in the formation of an SPV at the interface between the perovskite absorber and NiO$_x$ and the perovskite absorber appears to be intrinsic if one is not aware of the SPV. This light-induced shift on NiO$_x$ substrates was observed for FAPI, CsFAPI, MAFAPI, and CsMAFAPI perovskite films as well indicating that this is a general behavior for organic–inorganic lead halide perovskites. For the n$^+$-SnO$_2$/n-MAPI interface, no SPV was observed.

2.3. Determination of the Photovoltage Distribution throughout the Device

Having investigated the influence of the substrate material on the electronic structure of the perovskite absorber, the

devices are further completed by depositing the back contacts and finally a 25 nm thin gold film. PES measurements in the dark and under illumination are performed for the two classical architecture device stacks (ITO/n$^+$-SnO$_2$/MAPI/p-spiro-MeOTAD and ITO/n$^+$-SnO$_2$/MAPI/p-spiro-MeOTAD/Au) and for two inverted architecture device stacks (ITO/p-NiO$_x$/MAPI/C$_{60}$/BCP and ITO/p-NiO$_x$/MAPI/C$_{60}$/BCP/Au). By comparing the measurements of these four different device stacks, the interfaces at which the photovoltage is formed are identified for both architectures. For both architectures, the photovoltage appears at the n-MAPI/p-HEL interface. Furthermore, the results allow to construct full band diagrams for both architectures in the dark and under illumination (see **Figures 4** and **5**).

For the classical architecture, a doped spiro-MeOTAD film is spin-coated on top of the n$^+$-SnO$_2$/n-MAPI stack and the valence band region is measured in the dark and under illumination (see Figure 3a). In the dark, the VBM of spiro-MeOTAD appears at 0.64 eV and shifts by 0.66 eV to higher binding energies upon illumination, indicating a light-induced SPV which must be located at the n-MAPI/p-spiro-MeOTAD interface. Any other interface in the device stack below can be excluded as the origin of the SPV, since no light-induced shift was visible for the n$^+$-SnO$_2$/n-MAPI stack (see Figure 2a–c). Under illumination, the quasi-Fermi levels of electrons and holes split and a near flat band situation is induced, shifting the PES spectra to higher binding energies. Identifying the SPV of the classical architecture at the n-MAPI/p-spiro-MeOTAD interface is
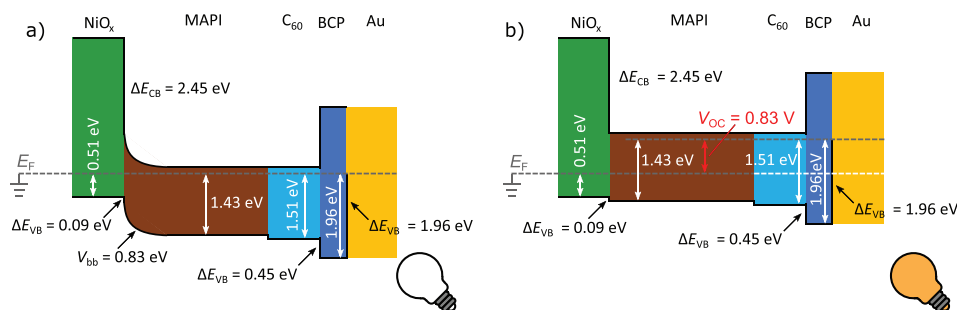

Figure 5. Schematic band diagrams derived from the PES measurements for devices in inverted architecture. a) In the dark with a band bending at the NiO$_x$/MAPI interface and b) under illumination with the band bending changing to a flat-band situation, giving rise to the V_{OC}. The white horizontal extension of the Fermi level in b) shows the Fermi level of the ground and therefore the reference energy for the PES measurements.

**ADVANCED
SCIENCE NEWS**
www.advancedsciencenews.com

**ADVANCED
ENERGY
MATERIALS**
www.advenergymat.de

consistent with the results for the inverted architecture, where an SPV of 0.70 eV appeared at the p-NiO$_x$/n-MAPI interface (see Figure 1d–f). The work functions of MAPI (4.02 eV) and spiro-MeOTAD (4.72 eV) differ by 0.70 eV (see Figure S4a, Supporting Information), which enables the formation of a built-in potential at this heterojunction and is in good agreement with the light-induced shift of 0.66 eV observed for the VBM. By performing a detailed analysis on the MAPI/spiro-MeOTAD interface a band bending inside the spiro-MeOTAD and a flat band inside the MAPI is identified (see Figure S7, Supporting Information). Furthermore, the interface experiment provides evidence that under illumination the band bending becomes flat, due to the formation of the SPV. The solar cell is finished by depositing a 25 nm gold contact on top of the spiro-MeOTAD layer and measuring the gold valence band (see Figure 3c). In the dark, the Fermi level appears at −0.04 eV, indicating that almost no X-ray-source-induced SPV is present. The illumination shifts the Fermi level by 0.80 eV to higher binding energies, which is a 0.14 eV higher shift compared to the n$^+$-SnO$_2$/n-MAPI/p-spiro-MeOTAD stack. This additional photovoltage of 0.14 V can be associated with the MAPI/spiro-MeOTAD as well as the spiro-MeOTAD/Au interface. Since a quasi-Fermi level splitting inside the spiro-MeOTAD without absorption seems rather unlikely, we attribute it in Figure 4 to the latter case. With 0.80 V, the photovoltage of the full device stack in PES appears somewhat lower compared to the V_{OC} of 1.05 V determined from the J-V-measurements using a solar simulator (see Figure S1, Supporting Information). The lower photovoltage in the PES measurements is explained by the lower light intensity (around 200 W m^{-2}) compared to the AM 1.5G spectrum (1000 W m^{-2}) since for the given experimental setup the sample is illuminated from the top through the gold. More information about the employed light source used to illuminate the samples during the PES measurements and the estimate of the light intensity reaching the perovskite absorber is given in chapter 10 of the Supporting Information. Therefore, the full photovoltage of the classical architecture device has been identified at the back contact (n-MAPI/p-spiro-MeOTAD/Au), which was already predicted in an earlier study, where the energy band diagram between MAPI and spiro-MeOTAD was investigated.[48] It is concluded that the classical architecture is an n$^+$-SnO$_2$/n-MAPI/p-spiro-MeOTAD structure and not an n-SnO$_2$/i-MAPI/p-spiro-MeOTAD structure as it is often referred to in literature.[15–17,19] In case of an n-i-p structure, the photovoltage would be split up between the SnO$_2$/MAPI and the MAPI/spiro-MeOTAD interface. This is obviously not the case, since only after the deposition of spiro-MeOTAD an SPV appears.

The inverted architecture (p-NiO$_x$/n-MAPI) is finished accordingly by depositing a 30 nm thick C$_{60}$ film followed by a 3 nm thick BCP buffer layer on top of the C$_{60}$ (see Figure 3b). In the dark, the C1s emission line appears at 285.11 eV and shifts by 0.72 eV to higher binding energies when turning on the light. The absolute value of this shift is almost identical to the shift that was observed for the p-NiO$_x$/n-MAPI stack (see Figure 2d–f), therefore indicating that by adding the n-EEL, the photovoltage does not further increase and no SPV forms at the n-MAPI/C$_{60}$/BCP contact. As no photovoltage at the n-MAPI/C$_{60}$/BCP contact is apparent, it is confirmed that the classical and inverted architectures function according to

the same working principle, i.e. with the photovoltage induced at the interface between n-MAPI and the p-HEL. Finally, a 25 nm gold film is deposited on top of the BCP to complete the device. The valence band spectra of the gold surface in the dark and under illumination are presented in Figure 3d. The Fermi level appears at −0.02 eV for the dark measurement, indicating that almost no X-ray-source-induced SPV is present. Under illumination, the Fermi level shifts by 0.83 eV to lower binding energies. This light-induced shift is 0.11 eV higher compared to the light-induced shift of the NiO$_x$/MAPI/C$_{60}$/BCP stack. As for the classical architecture, it is assumed (Figure 5) that the additional photovoltage of 0.11 V forms at the NiO$_x$/MAPI and not at the BCP/Au interface. The photovoltage of the completed device of 0.83 eV is comparable to the value that was observed for the classical architecture (0.80 eV) and somewhat lower than the typical V_{OC} extracted from J-V-measurements (1.03 eV, see Figure S1, Supporting Information). By comparing the light measurement for the classical and inverted structure, it is obvious that the binding energy shifts in opposite direction result from the formation of SPVs of opposite polarities. The fact that the large photovoltage for the inverted architecture is identified at the p-NiO$_x$/n-MAPI interface is in accordance with the observation for the classical architecture before. It is therefore concluded that the devices behave as n-n-p and p-n-n devices, instead of the commonly accepted idea of n-i-p and p-i-n devices.

2.4. Band Diagrams for the Classical and Inverted Architecture

Based on the presented measurements, band diagrams for the classical and inverted architecture in the dark and under illumination at open-circuit conditions are constructed for MAPI solar cells for the first time in literature (see Figure 4 for the classical architecture and Figure 5 for the inverted architecture).

Since no SPV is present at the SnO$_2$/MAPI interface (see Figure 2c), no band bending is present at this interface in the dark. With the VBM of SnO$_2$ (VBM$_{SnO_2}$ = 3.85 eV, see Figure S8a, Supporting Information) and MAPI (VBM$_{MAPI}$ = 1.35 eV, see Figure 2c), an offset of 2.32 eV between the VBM of MAPI and SnO$_2$ results (ΔE_{VB}), demonstrating an efficient blocking of holes. With the bandgaps of SnO$_2$ (E_{g,SnO_2} = 3.60 eV)[49] and MAPI ($E_{g,MAPI}$ = 1.58 eV),[48] the CBM of SnO$_2$ is positioned below the CBM of MAPI, which will allow electrons to be extracted from MAPI into the SnO$_2$ layer. Given the SPV of 0.80 eV at the MAPI/spiro-MeOTAD interface, it is concluded that a built-in potential of at least 0.80 eV exists at this interface for the dark case. A detailed analysis of the interface between MAPI and spiro-MeOTAD by co-depositing spiro-MeOTAD and LiTFSI on a MAPI surface shows that the band bending is present inside the spiro-MeOTAD (see Figure S7, Supporting Information). With the VBM of MAPI and spiro-MeOTAD measured at 1.35 and 0.64 eV, a valence band offset of 1.35 − 0.64 − 0.80 eV = −0.09 eV between both materials is expected. Given the VBM of 0.64 eV for spiro-MeOTAD, a maximum offset of 0.64 eV is predicted between the valence band of spiro-MeOTAD and the Au Fermi level. The corresponding schematic band diagram is presented in Figure 4a. From the band structure, it is apparent that the SnO$_2$ layer provides efficient hole blocking

**ADVANCED
SCIENCE NEWS**

www.advancedsciencenews.com

**ADVANCED
ENERGY
MATERIALS**

www.advenergymat.de

but does not contribute to the built-in field. In contrast, at the MAPI/spiro-MeOTAD interface efficient electron blocking is achieved by the energetically high lowest unoccupied molecular orbital (LUMO) level of spiro-MeOTAD and a built-in field can develop. The built-in potential (V_{bb}) of 0.80 eV is indicated by the curved line. The illuminated case at open-circuit conditions is presented in Figure 4b. At the MAPI/spiro-MeOTAD interface the band bending inside the spiro-MeOTAD is changing to a flat-band situation giving rise to the photovoltage, and a quasi-Fermi level splitting of the same magnitude appears inside the perovskite absorber. The white horizontal extension of the Fermi level shows the Fermi level of the grounded electron quasi-Fermi level, which is the reference energy for the PES measurements. By comparing the VBM of spiro-MeOTAD and the Fermi level of Au to the reference Fermi level of the ground (white broken line), it becomes evident why the SPV results in a shift of the core levels and the valence band spectra to higher binding energies.

The band diagram for the inverted architecture in the dark (see Figure 5a) is constructed accordingly. Since a photovoltage of 0.83 eV was assigned to the p-NiO_x/n-MAPI interface, a band bending of at least 0.83 eV exists at this interface. This band bending is drawn inside the MAPI and not the NiO_x, proven by a detailed study of this interface (see Figure S6, Supporting Information). The VBM of MAPI (1.43 eV, see Figure 2f) and NiO_x (0.53 eV, see Figure S8b, Supporting Information) differs by 0.90 eV, which results in a small valence band offset of 0.07 eV at this interface. The high offset of 2.07 eV between the CBM of NiO_x and MAPI (ΔE_{CB}) allows for an efficient electron blocking. As previously discussed, no additional photovoltage is identified at the n-MAPI/C_{60} interface, which is further verified by a detailed analysis of this interface in which no band bending has been observed (see Figure S9, Supporting Information). For the VBM of C_{60}, a value of 1.51 eV (see Figure S8c, Supporting Information) is determined. The band gap of C_{60} is assumed to be 1.67 eV.[50] This results in an aligned CBM of MAPI and LUMO of C_{60}. With the LUMO of BCP being 1.96 eV (see Figure S8c, Supporting Information) and a band gap of 3.5 eV,[51] a large offset between the LUMO of C_{60} and BCP is predicted. However, this will not block the electrons from entering the LUMO of BCP, since the BCP buffer layer has only a thickness of 3 nm, therefore allowing electrons to tunnel through it. The tunneling of electrons through gap states of the BCP has been described in literature elsewhere.[51–53] The band diagram for the inverted architecture under illumination is presented in Figure 5b.

In summary, for both architectures, the majority of the photovoltage is formed at the p-HEL/n-MAPI interface, which means that it is necessary to optimize the energetic alignments at these interfaces to further increase the V_{OC} and therefore also the PCE. Interestingly, the band bending is measured inside the perovskite absorber for the NiO_x/MAPI interface and inside the HEL in case of the MAPI/spiro-MeOTAD interface. In order to explain this different position of the band bending, the charge carrier concentrations of MAPI on SnO_2 and NiO_x are estimated. Wang et al.[23] reported a combined photoemission and Hall measurement study, relating VBM positions below the Fermi Level in photoemission to carrier concentrations from Hall measurements. For a perovskite film with the VBM of 1.3 eV below the Fermi level, an electron concentration of 7.6×10^{20} cm^{-3} was measured. As the VBM positions of the here presented perovskite films are slightly higher (1.35 and 1.43 eV for MAPI on SnO_2 and NiO_x, respectively), charge carrier concentrations of 2.0×10^{20} and 7×10^{20} cm^{-3} were extrapolated using their systematic data. The derived absolute values for the charge carrier concentrations are in conflict to high dark resistivity often measured for the perovskite films.[54,55] In addition, a charge carrier concentration of 2×10^{20} cm^{-3} for the MAPI perovskite on top of NiO_x would result in a rather small space charge region of around 3–5.6 nm only (see Chapter 11 of the Supporting Information for a detailed calculation). The derived charge carrier concentration values can therefore only be taken as rough estimates, as Hall measurements on thin MAPI perovskite films are challenging and the determination of the VBM in UPS is impeded by a low density of states near the onset of the valence band.[41] As the Fermi level position in the energy gap (measured in UPS as VBM position) enters exponentially in the calculation of the charge carrier concentration (see Chapter 12 of the Supporting Information), an uncertainty of the VBM position by 100 meV leads to almost an order of magnitude variation in the calculated carrier concentration both for the VBM measurements presented here as well as for Wang et al.[23] A dedicated cross-comparison of carrier concentrations derived from photoemission, Hall-measurements, and dark conductivity is needed in future.

Although there is a difference of a factor of around 3 in the doping levels, it is not expected that this difference can explain that the band bending is measured inside MAPI for the NiO_x/MAPI contact and inside spiro-MeOTAD for the MAPI/spiro-MeOTAD interface. The findings could be explained when it is assumed that for the NiO_x/MAPI interface, the alignment is determined by pinning of the NiO_x Fermi level to defect states at the nickel oxide surface, while the Fermi level in MAPI is free to move at this contact. On the other hand, the Fermi level is pinned at the MAPI surface, while it is free to move inside spiro-MeOTAD at the MAPI/spiro-MeOTAD contact. Other effects, like a compensation of the contact-induced electric field by ion migration at the MAPI/spiro-MeOTAD, but not at the NiO_x/MAPI contact may play a role as well.[56] Such mechanism was proposed for an external applied bias and may play a role as well for the contact-induced potentials as well. The fact that the work function difference between the HEL and the perovskite absorber defines the V_{OC} might explain why it is sometimes reported that the HEL variation has no or a small effect on the V_{OC}, since usually the effect of the ionization potential and not of the work function is investigated.[57–59] Thus, different HELs may have different ionization potentials, but similar Fermi level positions with respect to the perovskite Fermi level.

For the classical architecture, where the built-in potential is observed inside the spiro-MeOTAD, strategies to increase the photovoltage can either focus on i) increasing the built-in potential inside spiro-MeOTAD, or ii) moving the built-in potential into the perovskite absorber, as it is the case for the inverted architecture where NiO_x is used as HEL. Increasing the built-in potential inside spiro-MeOTAD should be possible by achieving a high work function difference between the perovskite absorber and spiro-MeOTAD. This can, e.g., be done by increasing the p-doping of spiro-MeOTAD (and therefore increasing its

**ADVANCED
SCIENCE NEWS**

www.advancedsciencenews.com

**ADVANCED
ENERGY
MATERIALS**

www.advenergymat.de

work function), or by employing a different HEL that already exhibits a larger work function. To move the built-in potential into the perovskite absorber, it is necessary to understand why it appears inside the spiro-MeOTAD and not inside the perovskite absorber. A reason for this can be the presence of gap states at the perovskite/spiro-MeOTAD interface, which results in a pinning of the Fermi level. Fermi level pinning can, e.g., be avoided by introducing buffer layers that passivate the gap states. Recently, several publications have reported empirically developed strategies to improve device performance, by employing such passivation layers at the perovskite/HEL interface.[34–38] However, the exact mechanism behind these passivation strategies is still not investigated in detail. The findings reported in this study may give a first understanding about the role of passivation layers at the perovskite/HEL interface.

3. Conclusion

In this work, novel insights into the working principle of PSCs have been developed by using a detailed PES study of its involved interfaces. Specific junctions, stacks, and completed solar cells in classical and inverted architecture were studied to identify at which interface the built-in potential is present in the dark and where the photovoltage is created under illumination. The SPVs of the full devices that were measured using PES are 0.80 and 0.83 V for the classical and inverted architectures, respectively. For both architectures, MAPI is measured as n-type and the vast majority of the V_{OC} is identified to appear at the p-type/n-MAPI interface. It is experimentally shown that the Fermi level inside MAPI is not influenced by the substrate it is grown on. The same behavior was also observed for FAPI, CsFAPI, MAFAPI, and CsMAFAPI perovskite absorbers. It is further observed that the lead halide perovskite interfaces are extremely sensitive to light and form an SPV even due to unintentional illumination, which can result in wrong data interpretation, since the perovskite is not measured in thermodynamic equilibrium. This unintentional non-equilibrium situation must be considered, not only when performing PES measurements on lead halide perovskites but in any measurements concerning Fermi level positioning in the dark and under illumination. Based on the PES results, an n+-SnO$_2$/n-MAPI/ p-spiro-MeOTAD device architecture and a p-NiO$_x$/n-MAPI/ C$_{60}$ device architecture is deduced for the devices with an n-p-heterojunction between MAPI and the respective p-HEL that is responsible for the solar cells V_{OC}. For a further improvement of the device open-circuit potential and the PCE, it is therefore recommended to focus on optimizing the MAPI/HEL contact. Especially, strong p-doping of the HEL and a low offset between the HEL ionization potential and the perovskite VBM with the HEL ionization potential just above the perovskite VBM should lead to better device performance. Additional photovoltage experiments should be performed on p-doped MAPI perovskite films to investigate that the photovoltage will be formed at the EEL/MAPI contact. The findings of this work should also be applicable for other perovskite absorbers (e.g., for wide band gap materials like CH$_3$NH$_3$PbBr$_3$), since their larger band gap compared to iodine-based perovskites is due to a lower lying VBM.

4. Experimental Section

All sample preparation took place at the Light Technology Institute at the Karlsruhe Institute of Technology (KIT). The devices investigated in this work were deposited on pre-patterned ITO substrates (Luminescence Technology Corp., CAS: 50926-11-9) that were cleaned consecutively in acetone (technical grade, VWR International, CAS: 67-64-1) and isopropanol (technical grade, VWR International, CAS: 67-63-0) in an ultrasonic bath for 10 min each. Right before the deposition of the first charge extracting layer, the substrates were cleaned in an oxygen plasma for 3 min. For the devices in classical architecture, SnO$_2$ was used as the electron extracting layer. The nanoparticular SnO$_2$ layer was fabricated by a solution-based approach discussed in a previous report.[60] For this, a commercial SnO$_2$ colloidal dispersion (15 wt% dispersion, Alfa Aesar, CAS: 18282-10-5) was diluted in deionized water to a concentration of 2 wt%. The deposition of the solution on top of the ITO front electrode was performed by spin coating at 4000 rpm for 30 s followed by an annealing at 250 °C for 30 min. The fabrication of the SnO$_2$ layer was carried out in ambient conditions. For the inverted architecture, magnetron-sputtered NiO$_x$ was used as HEL which was deposited on top of the ITO front electrode. Sputtering was performed in a PVD 75 PRO-Line system (Kurt J. Lesker Company) by employing a green NiO target (99.995% purity, Kurt J. Lesker Company, CAS: 1313-99-1) that was sputtered in a pure argon atmosphere at a process pressure of 1 mTorr and a power of 8 W in.$^{-2}$. The thickness of the NiO$_x$ layer was set to 20 nm.

To guarantee a sufficient homogeneity for the XPS investigations, vacuum-processed perovskite absorbers were used in this work. The deposition of the absorber was performed in a home-made evaporation system by simultaneously evaporating lead iodide (PbI$_2$, 99% purity, Sigma-Aldrich, CAS: 10101-63-0) and methylammonium iodide (MAI, GreatCell Solar, CAS: 14965-49-2). The stoichiometry of the resulting CH$_3$NH$_3$PbI$_3$ absorber films was controlled by the PbI$_2$ evaporation rate which was set to 0.3 Å s^{-1} for SnO$_2$ substrates or 0.5 Å s^{-1} for NiO$_x$ substrates and the MAI partial pressure which was held at 1.7×10^{-5} mbar for SnO$_2$ substrates or 3.0×10^{-5} mbar for NiO$_x$ substrates. During the deposition, the substrates were not actively cooled or heated. The thickness of the absorber was set to about 350 nm. Excess MAI on the surface of the absorber films was removed by a short post-treatment in isopropanol (99.5% anhydrous, Sigma-Aldrich, CAS: 67-63-0) in nitrogen atmosphere after the deposition. For further information about the vacuum-processed absorber fabrication, the reader is referred to previous reports.[13,61]

Solar cells in classical architecture were equipped with a doped spiro-MeOTAD layer on top of the absorber as the HEL. For this, 80 mg mL^{-1} of spiro-MeOTAD (Luminescence Technology Corp., CAS: 207739-72-8) was dissolved in chlorobenzene (99.8% anhydrous, Sigma-Aldrich, CAS: 108-90-7). After complete dissolution, 28.5 µL of 4-*tert*-butylpyridine (98% purity, Sigma-Aldrich, CAS: 3978-81-2) and 17.5 µL of a lithium stock solution were added to the solution. The lithium stock solution was prepared by dissolving 520 mg of bis(trifluoromethansulfonyl)imid (Sigma-Aldrich, CAS: 90076-65-6) in 1 mL of acetonitrile (99.8% anhydrous, Sigma-Aldrich, CAS: 75-05-8). The as-prepared solution was then deposited on top of the absorber by spin coating at 4000 rpm for 30 s in nitrogen atmosphere without any post-annealing. Devices employing spiro-MeOTAD as the HEL were kept in an oxygen atmosphere at 25% relative humidity for about 12 h. For devices based on the inverted architecture, a double layer of the fullerene C$_{60}$ (98% purity, Alfa Aesar, CAS: 99685-96-8) and BCP (Luminescence Technology Corp., CAS: 4733-39-5) was used as the EEL. Both layers were deposited by thermal evaporation in a Spectros evaporation system (Kurt J. Lesker Company). The 30 nm thick fullerene layer was deposited at an evaporation rate of about 0.2 Å s^{-1} whereas the 3 nm thick BCP layer was deposited at 0.4 Å s^{-1}. Finally, both device architectures were equipped with a 25 nm thick gold layer that was thermally evaporated at an evaporation rate of 2 Å s^{-1}.

Current–voltage characteristics of the solar cells were measured in a Newport solar simulator both in forward and backward scan

ADVANCED
SCIENCE NEWS

www.advancedsciencenews.com

ADVANCED
ENERGY
MATERIALS

www.advenergymat.de

direction under simulated AM1.5G light emitted from a xenon lamp. The intensity of the lamp was calibrated using a silicon reference solar cell equipped with a KG5 filter. The scan rate during the measurement was kept constant at 600 mV s^{-1}. The solar cells were actively cooled to a temperature of 25 °C during the measurement by means of a microcontroller-driven Peltier element.

For XRD investigations, a Bruker D8 DISCOVER system with Cu-K$_\alpha$ radiation was used in a Bragg-Brentano configuration.

The optical characteristics were extracted out of the transmittance and reflectance data, which were measured in a spectrophotometer (PerkinElmer Lambda 1050). Absorptance was calculated based on the measured reflectance and transmittance by using the formula $A = 1 - R - T$.

For the PES measurements, the samples were packed under nitrogen atmosphere and transported from the Karlsruhe Institute of Technology to the Technical University of Darmstadt (TUD). To be able to measure an SPV in the XPS analysis chamber, the samples were contacted to the electrical ground at the ITO contact, so the potential of all the other layers on top was electrically floating. For each sample, the light measurement was carried out first, followed by the dark measurement. For the light measurements, a 50 W ECONLUX SolarRaptor tungsten high-intensity discharge (HID)-lamp was attached to one of the glass view ports of the XPS measurement chamber and the sample was illuminated from a distance of roughly 50 cm at an angle of around 45°. Especially for the measurements of the full devices, the light intensity was attenuated before it could reach the perovskite absorber by absorption inside the gold film. More information on the used light source used to illuminate the samples during the PES measurements and an estimate of the light intensity reaching the perovskite absorber is given in Chapter 10 of the Supporting Information. For the dark measurements, the glass view ports of the vacuum chamber were covered with aluminum foil and all light sources inside the vacuum chamber, including the hot-filament ionization gauge, were turned off. An Al window positioned between the X-ray source and the sample was used to avoid that the visible light emitted by the electron emitter of the X-ray source could reach the sample. All XPS and UPS measurements were acquired with a monochromatic X-ray source (Al K-alpha) with an excitation energy of 1486.6 eV at a Thermo Fisher Escalab 250 or a Physical Electronics VersaProbe 5000. The spectra were calibrated to the Fermi level of silver (0 eV), the binding energy of the Au 4f$_{7/2}$ emission line (84.0 eV), the Ag 3d$_{5/2}$ emission line (368.26 eV), and the Cu 2p$_{3/2}$ emission line (932.67 eV). The UPS measurements were calibrated using the Fermi level of gold (0 eV). All calibration samples were cleaned with an argon sputter gun before the measurement. The VBM values of semiconductors were determined by applying a linear fit to the valence band onset and the background and taking the intersection between both lines. The Fermi level value of metal surfaces was determined with a Sigmoid fit and taking the position where the intensity is at 50%.

Supporting Information

Supporting Information is available from the Wiley Online Library or from the author.

Conflict of Interest

The authors declare no conflict of interest.

[1] NREL, Best Research-Cell Efficiency Chart, https://www.nrel.gov/pv/assets/pdfs/best-research-cell-efficiencies.20200803.pdf (accessed: August 2020).

[2] I. A. Howard, T. Abzieher, I. M. Hossain, H. Eggers, F. Schackmar, S. Ternes, B. S. Richards, U. Lemmer, U. W. Paetzold, Adv. Mater. 2019, 31, 1806702.

[3] E. J. Juarez-Perez, M. Wussler, F. Fabregat-Santiago, K. Lakus-Wollny, E. Mankel, T. Mayer, W. Jaegermann, I. Mora-Sero, J. Phys. Chem. Lett. 2014, 5, 680.

[4] M. Stolterfoht, P. Caprioglio, C. M. Wolff, J. A. Marquez, J. Nordmann, S. S. Zhang, D. Rothhardt, U. Hormann, Y. Amir, A. Redinger, L. Kegelmann, F. S. Zu, S. Albrecht, N. Koch, T. Kirchartz, M. Saliba, T. Unold, D. Neher, Energy Environ. Sci. 2019, 12, 2778.

[5] C. M. Wolff, P. Caprioglio, M. Stolterfoht, D. Neher, Adv. Mater. 2019, 31, 1902762.

[6] W. B. Yan, Y. L. Li, Y. Li, S. Y. Ye, Z. W. Liu, S. F. Wang, Z. Q. Bian, C. H. Huang, Nano Energy 2015, 16, 428.

[7] J. P. Correa-Baena, W. Tress, K. Domanski, E. H. Anaraki, S. H. Turren-Cruz, B. Roose, P. P. Boix, M. Gratzel, M. Saliba, A. Abate, A. Hagfeldt, Energy Environ. Sci. 2017, 10, 1207.

[8] L. E. Polander, P. Pahner, M. Schwarze, M. Saalfrank, C. Koerner, K. Leo, APL Mater. 2014, 2, 081503.

[9] Q. Jiang, X. W. Zhang, J. B. You, Small 2018, 14, 1801154.

[10] R. Singh, P. K. Singh, B. Bhattacharya, H. W. Rhee, Appl. Mater. Today 2019, 14, 175.

[11] C. Rodriguez-Seco, L. Cabau, A. Vidal-Ferran, E. Palomares, Acc. Chem. Res. 2018, 51, 869.

[12] S. Ameen, M. A. Rub, S. A. Kosa, K. A. Alamry, M. S. Akhtar, H. S. Shin, H. K. Seo, A. M. Asiri, M. K. Nazeeruddin, ChemSusChem 2016, 9, 10.

[13] T. Abzieher, S. Moghadamzadeh, F. Schackmar, H. Eggers, F. Sutterluti, A. Farooq, D. Kojda, K. Habicht, R. Schmager, A. Mertens, R. Azmi, L. Klohr, J. A. Schwenzer, M. Hetterich, U. Lemmer, B. S. Richards, M. Powalla, U. W. Paetzold, Adv. Energy Mater. 2019, 9, 1802995.

[14] F. Behrouznejad, S. Shahbazi, N. Taghavinia, H. P. Wu, E. W. G. Diau, J. Mater. Chem. A 2016, 4, 13488.

[15] E. Edri, S. Kirmayer, A. Henning, S. Mukhopadhyay, K. Gartsman, Y. Rosenwaks, G. Hodes, D. Cahen, Nano Lett. 2014, 14, 1000.

[16] V. W. Bergmann, S. A. L. Weber, F. J. Ramos, M. K. Nazeeruddin, M. Gratzel, D. Li, A. L. Domanski, I. Lieberwirth, S. Ahmad, R. Berger, Nat. Commun. 2014, 5, 5001.

[17] I. M. Hermes, Y. Hou, V. W. Bergmann, C. J. Brabec, S. A. L. Weber, J. Phys. Chem. Lett. 2018, 9, 6249.

[18] L. Barnea-Nehoshtan, S. Kirmayer, E. Edri, G. Hodes, D. Cahen, J. Phys. Chem. Lett. 2014, 5, 2408.

[19] J. R. Harwell, T. K. Baikie, I. D. Baikie, J. L. Payne, C. Ni, J. T. S. Irvine, G. A. Turnbull, I. D. W. Samuel, *Phys. Chem. Chem. Phys.* **2016**, *18*, 19738.

[20] M. L. Cai, N. Ishida, X. Li, X. D. Yang, T. Noda, Y. Z. Wu, F. X. Xie, H. Naito, D. Fujita, L. Y. Han, *Joule* **2018**, *2*, 296.

[21] B. Danekamp, C. Muller, M. Sendner, P. P. Boix, M. Sessolo, R. Lovrincic, H. J. Bolink, *J. Phys. Chem. Lett.* **2018**, *9*, 2770.

[22] P. Fassl, V. Lami, A. Bausch, Z. P. Wang, M. T. Klug, H. J. Snaith, Y. Vaynzof, *Energy Environ. Sci.* **2018**, *11*, 3380.

[23] Q. Wang, Y. C. Shao, H. P. Xie, L. Lyu, X. L. Liu, Y. L. Gao, J. S. Huang, *Appl. Phys. Lett.* **2014**, *105*, 163508.

[24] D. D. Song, P. Cui, T. Y. Wang, D. Wei, M. C. Li, F. H. Cao, X. P. Yue, P. F. Fu, Y. Y. Li, Y. He, B. Jiang, M. Trevor, *J. Phys. Chem. C* **2015**, *119*, 22812.

[25] J. E. Demuth, W. J. Thompson, N. J. Dinardo, R. Imbihl, *Phys. Rev. Lett.* **1986**, *56*, 1408.

[26] M. Alonso, R. Cimino, K. Horn, *Phys. Rev. Lett.* **1990**, *64*, 1947.

[27] E. M. Miller, Y. X. Zhao, C. C. Mercado, S. K. Saha, J. M. Luther, K. Zhu, V. Stevanovic, C. L. Perkins, J. van de Lagemaat, *Phys. Chem. Chem. Phys.* **2014**, *16*, 22122.

[28] S. Olthof, K. Meerholz, *Sci. Rep.* **2017**, *7*, 40267.

[29] Y. Zou, Q. Meng, H. Y. Mao, D. B. Zhu, *Org. Electron.* **2017**, *41*, 307.

[30] C. G. Wang, C. C. Wang, X. L. Liu, J. Kauppi, Y. C. Shao, Z. G. Xiao, C. Bi, J. S. Huang, Y. L. Gao, *Appl. Phys. Lett.* **2015**, *106*, 111603.

[31] F. S. Zu, C. M. Wolff, M. Ralaiarisoa, P. Amsalem, D. Neher, N. Koch, *ACS Appl. Mater. Interfaces* **2019**, *11*, 21578.

[32] A. Klein, T. Mayer, A. Thissen, W. Jaegermann, in *Methods in Physical Chemistry* (Eds: R. Schäfer, P. C. Schmidt), Wiley, New York **2012**, pp 477.

[33] M. Wussler, T. Mayer, C. Das, E. Mankel, T. Hellmann, C. Prawobo, I. Zimmermann, M. K. Nazeeruddin, W. Jaegermann, *Adv. Funct. Mater.* **2020**, *30*, 1910679.

[34] B. Chaudhary, A. Kulkarni, A. K. Jena, M. Ikegami, Y. Udagawa, H. Kunugita, K. Ema, T. Miyasaka, *ChemSusChem* **2017**, *10*, 2473.

[35] L. J. Zuo, H. X. Guo, D. W. deQuilettes, S. Jariwala, N. De Marco, S. Q. Dong, R. DeBlock, D. S. Ginger, B. Dunn, M. K. Wang, Y. Yang, *Sci. Adv.* **2017**, *3*, e1700106.

[36] H. Kanda, N. Shibayama, A. J. Huckaba, Y. Lee, S. Paek, N. Klipfel, C. Roldan-Carmona, V. I. E. Queloz, G. Grancini, Y. Zhang, M. Abuhelaiga, K. T. Cho, M. Li, M. D. Mensi, S. Kinge, M. K. Nazeeruddin, *Energy Environ. Sci.* **2020**, *13*, 1222.

[37] N. K. Noel, S. N. Habisreutinger, A. Pellaroque, F. Pulvirenti, B. Wenger, F. Zhang, Y. H. Lin, O. G. Reid, J. Leisen, Y. Zhang, S. Barlow, S. R. Marder, A. Kahn, H. J. Snaith, C. B. Arnold, B. P. Rand, *Energy Environ. Sci.* **2019**, *12*, 3063.

[38] S. Gharibzadeh, B. A. Nejand, M. Jakoby, T. Abzieher, D. Hauschild, S. Moghadamzadeh, J. A. Schwenzer, P. Brenner, R. Schmager, A. A. Haghighirad, L. Weinhardt, U. Lemmer, B. S. Richards, I. A. Howard, U. W. Paetzold, *Adv. Energy Mater.* **2019**, *9*, 1803699.

[39] D. Mao, A. Kahn, M. Marsi, G. Margaritondo, *Appl. Surf. Sci.* **1991**, *48–49*, 324.

[40] J. P. Long, V. M. Bermudez, *Phys. Rev. B* **2002**, *66*, 121308.

[41] J. Endres, D. A. Egger, M. Kulbak, R. A. Kerner, L. F. Zhao, S. H. Silver, G. Hodes, B. P. Rand, D. Cahen, L. Kronik, A. Kahn, *J. Phys. Chem. Lett.* **2016**, *7*, 2722.

[42] P. Schulz, E. Edri, S. Kirmayer, G. Hodes, D. Cahen, A. Kahn, *Energy Environ. Sci.* **2014**, *7*, 1377.

[43] F. S. Zu, P. Amsalem, D. A. Egger, R. B. Wang, C. M. Wolff, H. H. Fang, M. A. Loi, D. Neher, L. Kronik, S. Duhm, N. Koch, *J. Phys. Chem. Lett.* **2019**, *10*, 601.

[44] Z. Hawash, S. R. Raga, D. Y. Son, L. K. Ono, N. G. Park, Y. B. Qi, *J. Phys. Chem. Lett.* **2017**, *8*, 3947.

[45] L. Li, S. C. Tong, Y. Zhao, C. Wang, S. T. Wang, L. Lyu, Y. B. Huang, H. Huang, J. L. Yang, D. M. Niu, X. L. Liu, Y. L. Gao, *ACS Appl. Mater. Interfaces* **2018**, *10*, 20959.

[46] X. N. Zhang, Z. H. Su, B. Zhao, Y. G. Yang, Y. M. Xiong, X. Y. Gao, D. C. Qi, L. Cao, *Appl. Phys. Lett.* **2018**, *113*, 113901.

[47] P. Schulz, L. L. Whittaker-Brooks, B. A. MacLeod, D. C. Olson, Y. L. Loo, A. Kahn, *Adv. Mater. Interfaces* **2015**, *2*, 1400532.

[48] T. Hellmann, M. Wussler, C. Das, R. Dachauer, I. El-Helaly, C. Mortan, T. Mayer, W. Jaegermann, *J. Mater. Chem. C* **2019**, *7*, 5324.

[49] K. Reimann, M. Steube, *Solid State Commun.* **1998**, *105*, 649.

[50] K. C. Chiu, J. S. Wang, C. Y. Lin, *J. Appl. Phys.* **1996**, *79*, 1784.

[51] H. Yoshida, *J. Phys. Chem. C* **2015**, *119*, 24459.

[52] T. Sakurai, S. Toyoshima, H. Kitazume, S. Masuda, H. Kato, K. Akimoto, *J. Appl. Phys.* **2010**, *107*, 043707.

[53] J. Lee, S. Park, Y. Lee, H. Kim, D. Shin, J. Jeong, K. Jeong, S. W. Cho, H. Lee, Y. Yi, *Phys. Chem. Chem. Phys.* **2016**, *18*, 5444.

[54] Y. L. Song, W. H. Bi, A. R. Wang, X. T. Liu, Y. F. Kang, Q. F. Dong, *Nat. Commun.* **2020**, *11*, 274.

[55] Y. Chen, H. T. Yi, X. Wu, R. Haroldson, Y. N. Gartstein, Y. I. Rodionov, K. S. Tikhonov, A. Zakhidov, X. Y. Zhu, V. Podzorov, *Nat. Commun.* **2016**, *7*, 12253.

[56] S. A. L. Weber, I. M. Hermes, S. H. Turren-Cruz, C. Gort, V. W. Bergmann, L. Gilson, A. Hagfeldt, M. Graetzel, W. Tress, R. Berger, *Energy Environ. Sci.* **2018**, *11*, 2404.

[57] B. Danekamp, N. Droseros, D. Tsokkou, V. Brehm, P. P. Boix, M. Sessolo, N. Banerji, H. J. Bolink, *J. Mater. Chem. C* **2019**, *7*, 523.

[58] J. Jimenez-Lopez, W. Cambarau, L. Cabau, E. Palomares, *Sci. Rep.* **2017**, *7*, 6101.

[59] R. A. Belisle, P. Jain, R. Prasanna, T. Leijtens, M. D. McGehee, *ACS Energy Lett.* **2016**, *1*, 556.

[60] J. A. Schwenzer, L. Rakocevic, R. Gehlhaar, T. Abzieher, S. Gharibzadeh, S. Moghadamzadeh, A. Quintilla, B. S. Richards, U. Lemmer, U. W. Paetzold, *ACS Appl. Mater. Interfaces* **2018**, *10*, 16390.

[61] T. Abzieher, J. A. Schwenzer, S. Moghadamzadeh, F. Sutterluti, I. M. Hossain, M. Pfau, E. Lotter, M. Hetterich, B. S. Richards, U. Lemmer, M. Powalla, U. W. Paetzold, *IEEE J. Photovoltaics* **2019**, *9*, 1249.